



## The Dynamics of Quasigeostrophic Lens-Shaped Vortices

BENJAMIN A. STORER AND FRANCIS J. POULIN

*Department of Applied Mathematics, University of Waterloo, Waterloo, Ontario, Canada*

CLAIRE MÉNESGUEN

*Laboratoire d'Océanographie Physique et Spatiale, UMR 6523, CNRS, IFREMER, IRD, UBO, Plouzane, France*

(Manuscript received 1 March 2017, in final form 13 December 2017)

### ABSTRACT

The stability of lens-shaped vortices is revisited in the context of an idealized quasigeostrophic model. We compute the stability characteristics with higher accuracy and for a wider range of Burger numbers ( $Bu$ ) than what was previously done. It is found that there are four distinct  $Bu$  regions of linear instability. Over the primary region of interest ( $0.1 < Bu < 10$ ), we confirm that the first and second azimuthal modes are the only linearly unstable modes, and they are associated with vortex tilting and tearing, respectively. Moreover, the most unstable first azimuthal mode is not precisely captured by the linear stability analysis because of the extra condition that is imposed at the vortex center, and accurate calculations of the second azimuthal mode require higher resolution than was previously considered. We also study the nonlinear evolution of lens-shaped vortices in the context of this model and present the following results. First, vortices with a horizontal length scale a little less than the radius of deformation ( $Bu > 1$ ) are barotropically unstable and develop a wobble, whereas those with a larger horizontal length scale ( $Bu < 1$ ) are baroclinically unstable and often split. Second, the transfer of energy between different horizontal scales is quantified in two typical cases of barotropic and baroclinic instability. Third, after the instability the effective  $Bu$  is closer to unity.

### 1. Introduction

The dynamical importance of interior mesoscale eddies in the oceanic energy budget and transport is well documented in the literature and excellent reviews can be found in [McWilliams \(1985\)](#) and [Carton \(2001\)](#). Examples of deep mesoscale eddies can be found west of the Strait of Gibraltar where a bottom-dwelling current detaches from the floor at a level of neutral buoyancy. The high speeds of this current lead to the formation of vortices, which are both warm and salty since the source water originates from the Mediterranean Sea ([Serra et al. 2005](#); [Aiki and Yamagata 2004](#)). These Mediterranean eddies are predominantly anticyclonic in nature and are referred to as Meddies. Other examples of subsurface mesoscale eddies can be found in the Arctic Canadian Basin, recently investigated by [Zhao and Timmermans \(2015\)](#), the Red Sea (Reddies), the Persian Gulf (Peddies), and others [see

[Ciani \(2016\)](#) and [Ciani et al. \(2015\)](#) for a review of surface and interior mesoscale lens vortices].

Meddies are long-lived features that may collapse on sea mounts or remain coherent and cross the Atlantic Ocean ([Serra et al. 2002](#); [Serra and Ambar 2002](#)). Observations estimate the lifespan of Meddies to be approximately one year for those that impact sea mounts and four years otherwise; as many as 29 Meddies can be expected to exist at any given time ([Richardson et al. 2000](#)). [Prater and Sanford \(1994, their Fig. 19\)](#) suggest that a reasonable range of Burger ( $Bu$ ) and Rossby ( $Ro$ ) numbers for mature Meddies is  $0.1 < Bu < 0.5$  and  $-0.5 < Ro < -0.1$ , with some observed Meddies falling outside that range. There are relatively few observations of recently formed Meddies compared to mature Meddies that are found propagating far from the coastlines in the Atlantic Ocean. Meddies that are observed over many months are presumably quite stable and would only permit very slowly growing perturbations. The analysis in this manuscript goes beyond the Meddy regime and considers a significantly wider parameter range. Moreover, we are looking to qualitatively

*Corresponding author:* Benjamin A. Storer, [bastorer@uwaterloo.ca](mailto:bastorer@uwaterloo.ca)

identify the instabilities, which is why we idealize the Meddy shape into a simplified baroclinic Gaussian lens.

Motivated by the nature of Meddies, Arctic eddies, Reddies, and Peddies, we investigate the stability of lens-shaped vortices over a wide range of Burger numbers. Previously, with a focus on Meddies, [Nguyen et al. \(2012\)](#) did a linear stability analysis (LSA) for lens-shaped vortices in the context of the quasigeostrophic (QG) model. They determined that there were different types of instabilities that could occur depending on the Bu. Our results focus on the same vortex solution in the QG model and confirm many of their conclusions but also better refine some of their findings, thereby giving us a more accurate picture of the linear stability characteristics of this particular type of vortex. Subsequently, the dynamics of these lens-shaped vortices was studied in the non-hydrostatic primitive equations for a wide range of Rossby, Froude (or Burger), and Reynolds numbers, in the context of nonhydrostatic Boussinesq equations ([Mahdinia et al. 2016](#); [Yim et al. 2016](#)). They identified many more different types of instabilities that can occur, but they focused on the dissipative dynamics and therefore did not quite touch on the regime on which we focus.

It will be shown that in the QG model there are primarily four distinct regions of linear instability in parameter space, and they are (where  $k_\theta$  is the azimuthal wavenumber) 1)  $1 < \text{Bu} < 10$ , where  $k_\theta = 1$  is the only unstable mode, is associated with vortex tilting, and is not accurately described by the linear theory presented here or in [Nguyen et al. \(2012\)](#); 2)  $\text{Bu} \gg 1$ , where both  $k_\theta = 1, 2$  are unstable; 3)  $0.1 < \text{Bu} < 1$ , where  $k_\theta = 2$  is the only unstable mode, is connected to vortex tearing events, and requires higher resolution than was used in previous results; and 4)  $\text{Bu} < 0.1$ , where there are many unstable modes, but we note that this is reaching beyond the QG limits.

The paper is organized as follows. [Section 2](#) presents the problem formulation, model equations, and initial conditions that are considered. [Section 3](#) discusses the linear stability analysis and compares our results with previous works. [Section 4](#) considers two specific fully nonlinear three-dimensional simulations and provides an in-depth discussion of the time evolution. Azimuthal decompositions of the nonlinear simulations are presented in [section 4c](#). [Section 4d](#) considers the energetics and growth rates for a suite of nonlinear simulations. Power spectra and wavelength-dependent rates of change of energy for selected simulations are then discussed in [section 4e](#). Conclusions and discussion are in [section 5](#).

## 2. Model equations and numerical methods

In this section we present the continuously stratified QG model as well as the equations for the linear stability

problem. The details of the numerical methods for both the linear stability calculations and nonlinear simulations are provided.

### a. Quasigeostrophic equations

For the QG model to be valid, it is sufficient that the Rossby number and aspect ratio are small and the Burger number is order one ([Vallis 2006](#), p. 207). In its conservative form, it states that potential vorticity (PV) is conserved following the flow [[Eq. \(1\)](#)], the PV is a sum of the relative vorticity and vertical stretching [[Eq. \(2\)](#)], and the leading-order velocity is in geostrophic balance [[Eq. \(3\)](#)]. In the following, the partial symbols denote partial derivatives,  $q$  denotes the potential vorticity,  $\mathbf{u}_H$  denotes the horizontal velocity vector,  $\nabla_H$  is the horizontal gradient operator,  $\nabla_H^2$  is the horizontal Laplace operator,  $\psi$  is the streamfunction,  $\hat{\mathbf{z}}$  is the vertical unit vector,  $f_0$  is the constant Coriolis frequency corresponding to the  $f$ -plane assumption, and  $N_0$  is the constant buoyancy frequency:

$$\partial_t q + \mathbf{u}_H \cdot \nabla_H q = 0, \quad (1)$$

$$q = \left( \nabla_H^2 + \frac{f_0^2}{N_0^2} \partial_{zz} \right) \psi, \quad \text{and} \quad (2)$$

$$(\mathbf{u}, \mathbf{v}) = \hat{\mathbf{z}} \times \nabla \psi. \quad (3)$$

### b. Initial conditions

The physical geometry is chosen to be the rectangular domain given by  $x \in [-(1/2)L_x, (1/2)L_x]$ ,  $y \in [-(1/2)L_y, (1/2)L_y]$ , and  $z \in [-L_z, 0]$ . The lens-shaped vortex has horizontal and vertical length scales of  $L_h$  and  $L_v$ , respectively. A list of model parameters is given in [Table 1](#). We choose to nondimensionalize space using these length scales around the center of the vortex  $[0, 0, -(1/2)L_z]$ :

$$(\tilde{x}, \tilde{y}, \tilde{z}) = \left( \frac{x}{L_h}, \frac{y}{L_h}, \frac{z + \frac{1}{2}L_z}{L_v} \right).$$

We choose the nondimensional parameter in the QG model to be the Burger number, which can be written as  $\text{Bu} = (L_D/L_h)^2$  with a deformation radius of  $L_D = N_0 L_v / f_0$ . For a particular Bu, one can then determine the corresponding horizontal length scale using  $L_h = (N_0 L_v) / (f_0 \sqrt{\text{Bu}})$ . While the derivation of the QG model requires a very small Rossby number, since the basic state has a nonzero velocity we can define an associated Rossby number and relate them by  $U_0 = f_0 L_h \text{Ro}$ . The dimensional PV in terms of the nondimensional coordinates is given by

TABLE 1. Description of parameters and notation.

Parameter	Dimensions	Description
$L_h$	m	Horizontal length scale of the vortex
$L_v$	m	Vertical length scale of the vortex
$N_0$	$s^{-1}$	Buoyancy (Brunt–Väisälä) frequency
$f_0$	$s^{-1}$	Coriolis $f$ -plane parameter
$U_0$	$m s^{-1}$	Characteristic velocity of the vortex
Bu	Dimensionless	Burger number = $[(N_0 L_v)/(f_0 L_h)]^2$
$x, y, z$	m	Dimensional Cartesian coordinates
$\tilde{x}, \tilde{y}, \tilde{z}$	Dimensionless	Nondimensional Cartesian coordinates
$q$	$s^{-1}$	Potential vorticity
$\psi$	$m^2 s^{-1}$	Streamfunction
$Q$	$s^{-1}$	Background potential vorticity
$\Psi$	$m^2 s^{-1}$	Background streamfunction
$k_\theta$	Dimensionless	Azimuthal mode number

$$q = -\frac{U_0}{L_h} \left[ \tilde{r}^2 - 1 + \frac{1}{\text{Bu}} (\tilde{z}^2 - 0.5) \right] e^{(-\tilde{r}^2 - \tilde{z}^2)}, \quad (4)$$

where  $\tilde{r}^2 = \tilde{x}^2 + \tilde{y}^2$ . Dimensional values that are appropriate for Meddies are  $f_0 = 8 \times 10^{-5} s^{-1}$ ,  $N_0 = \sqrt{5} \times 10^{-5} s^{-1}$ ,  $U_0 = 0.25 m s^{-1}$ , and  $L_v = 400 m$  (Hua et al. 2013), corresponding to a deformation radius of  $L_d \approx 11 km$ . In this investigation we consider  $O(1) \leq L_h \leq O(100) km$ . A summary of the parameters used in the nonlinear simulations is in Table 2.

c. Formulation and numerical method for linear stability problem

The generalized eigenvalue problem is given by Eq. (A1), the derivation of which can be found in the appendix. The spectrum of the generalized eigenvalue problem is computed with an indirect Krylov method implemented using the Scalable Library for Eigenvalue Problem Computations (SLEPc). A fourth-order finite-difference scheme is used to discretize both the radial and vertical spatial derivatives. To speed up convergence on higher-resolution grids, seed values were provided from calculations on coarser grids. It is important to note that the linear stability computations use cylindrical coordinates centered about the vortex core and are achieved for a given azimuthal mode number  $k_\theta$ . Doing so reduces the problem to two dimensions, greatly simplifying the numerical calculations at the cost of added boundary condition at  $r = 0$ .

The boundary conditions at the rigid lid and flat bottom is zero buoyancy, which ensures that there is no vertical velocity through the boundaries. Written in terms of the streamfunction, this becomes  $\partial_z \psi = 0$  at  $z = -L_z, 0$  (Nguyen et al. 2012). As discussed in Baey and Carton (2002), the condition at  $r = 0$  is that the pressure anomaly vanishes,  $\psi = 0$ , for all nonzero azimuthal mode numbers. This can be obtained from Yim

(2015) in the QG limit. Furthermore, the streamfunction is assumed to vanish in the far field, yielding  $\psi = 0$  at  $r = L_r$ .

d. Numerical method for the nonlinear dynamics

Nonlinear simulations are performed using the Spectral Parallel Incompressible Navier–Stokes Solver (SPINS) model (Subich et al. 2013), which uses spectral

TABLE 2. Simulation parameters. In each simulation, the following physical parameters are held constant:  $f_0 = 0.8 \times 10^{-4} s^{-1}$ ,  $N_0 = \sqrt{5} \times 10^{-3} s^{-1}$ , and  $L_v = 400 m$ . Note that the linear stratification corresponds to a total density change of less than 1%. The filter parameters were  $\alpha = 20, \beta = 2$ , and  $\kappa_{\text{cut}} = 0.7$ , indicating that 70% of the wavenumbers are unchanged.

Bu	$N_x, N_y, N_z$	$L_h$ (m)	$L_x, L_y$ (m)	$L_z$ (m)
0.01	512	111 803.0	2 236 070.0	4000
0.03	256	64 549.7	1 290 990.0	3000
0.05	256	50 000.0	650 000.0	3000
0.1	256	35 355.3	707 107.0	3000
0.14	512	29 880.7	448 211.0	3000
0.22	256	23 836.6	476 731.0	3000
0.3125	256	20 000.0	400 000.0	3000
0.4	256	17 677.7	353 553.0	3000
0.5	256	15 811.4	316 228.0	3000
0.6	256	14 433.8	288 675.0	3000
0.75	256	12 909.9	258 199.0	3000
1.2	256	10 206.2	204 124.0	3000
1.54	256	9 009.37	180 187.0	3000
2.0	256	7 905.69	158 114.0	3000
3.0	256	6 454.97	129 099.0	3000
4.0	256	5 590.17	111 803.0	3000
5.0	256	5 000.0	100 000.0	3000
7.0	256	4 225.77	84 515.4	3000
10.0	256	3 535.53	70 710.7	3000
15.8489	256	2 808.37	56 167.5	3000
25.1189	256	2 230.77	44 615.4	3000
39.8107	256	1 771.96	35 439.3	3000
63.0957	256	1 407.52	28 150.4	3000
100.0	256	1 118.03	22 360.7	3000

collocation methods to numerically integrate the non-hydrostatic and incompressible Navier–Stokes equations. To perform simulations using QG dynamics, the authors developed a QG variant of the SPINS code, which integrates the three-dimensional, linearly stratified, QG equations (B. Storer et al. 2018, unpublished manuscript). Specifically, the code solves Eq. (1) using an adaptive third-order Adams–Bashforth scheme for the time stepping, fast Fourier transforms (FFTs) in each horizontal direction and a discrete cosine transform (DCT) in the vertical for the streamfunction. The horizontal FFTs correspond to periodic boundary conditions in  $x$  and  $y$ , while the DCT in the vertical corresponds to rigid-lid and free slip conditions in  $z$ . In contrast to the LSA calculations, no conditions are imposed at  $r = \sqrt{x^2 + y^2} = 0$ . To maintain nearly inviscid dynamics, the model equations do not include any viscous terms. To ensure numerical stability, an exponential filter is applied to remove energy from all wavenumbers that exceed a specified cut-off.

### 3. Linear stability analysis: Dependence on the Burger number

To better understand the types of lens vortices that can remain coherent for a long span of time, we begin with linear stability analysis. This analysis is presented here, not as the focus of the study but to provide context for the nonlinear results.

Using the method discussed in section 2c, linear stability calculations are performed over a broad range of Burger numbers, with 250 points distributed logarithmically over  $10^{-2} < \text{Bu} < 10$  and 75 points over  $10 < \text{Bu} < 10^2$ . The results of our calculations will be compared with previous studies of linear stability as well as the growth rates estimated by the fully nonlinear simulations presented in this paper.

Nguyen et al. (2012) found that there were three different ranges of Burger number that yield qualitatively different behaviors. The different stability characteristics in the regimes are well illustrated in their Figs. 1a,c. If  $\text{Bu} = 1$ , it is shown that the eddy is stable, indicating that the vortex scale is equal to that of the Rossby radius of deformation,  $L_h = L_D = N_0 L_v / f_0$ . If  $\text{Bu} < 1$  ( $\text{Bu} > 1$ ), corresponding to vortices larger (smaller) than the deformation radius, the most unstable wave has a mode 2 (mode 1) in the azimuthal direction with a symmetric (asymmetric) structure in the vertical. Figure 1c in Nguyen et al. (2012) focuses on the regime of very large length scales and shows that there are multiple unstable modes,  $k_\theta \in \{1, 2, 3, 4, 5\}$ , and that their growth rates ( $\sigma$ ) are comparable, with  $0.03 < \sigma(4/\text{Ro}) < 0.05$ .

We confirm that the linear stability results of Nguyen et al. (2012) are robust using calculations with greater

accuracy by making two important changes: we use fourth-order discretization as well as a spatial resolution of  $1024 \times 1024$ , which is roughly 10 times finer than what they present. In general we find good qualitative agreement in the range of  $\text{Bu}$  that they considered, although we find that there are four different regions of instability. Through doing a convergence study we determined that the results presented in Fig. 1 are robust; the only exceptions are the growth rates for  $k_\theta = 3, 4, 5$  when the growth rate is below  $2 \times 10^{-2}$ .

#### a. Growth rates of eigenmodes and comparisons to previous works

Figure 1 presents a summary of both the linear and nonlinear growth-rate analyses. The linear stability analysis is plotted in small dots for the first five nonzero azimuthal modes, showing only the fastest-growing instability for each azimuthal mode. Squares indicate estimates of the growth rates produced by Nguyen et al. (2012), with grid resolution of  $100 \times 100$ , and large circles show the growth rates predicted by the nonlinear simulations in QG SPINS (see section 4d).

- (i) For very large vortices ( $\text{Bu} < 10^{-1}$ ) the LSA reveals that  $k_\theta = 1, 2, 3, 4, 5$  are each unstable with roughly comparable growth rates as  $\text{Bu} \rightarrow 10^{-2}$ . In the nonlinear simulation with  $\text{Bu} = 10^{-2}$  (not shown) it was determined that the first five azimuthal modes were the only ones that experienced exponential growth at the early stages. This is the rationale for only considering these modes in the linear stability analysis since these calculations were computationally demanding. The stability of  $k_\theta = 3, 4, 5$  is computed for the full parameter range, but they were only found to be unstable for very small Burger numbers and are stable in each of the following regimes.
- (ii) For moderately large vortices ( $10^{-1} < \text{Bu} < 1$ ) the primary instability has a  $k_\theta = 2$  structure and is vertically symmetric about the middepth (see Fig. 3a; below). Throughout, the growth rates computed from the nonlinear simulations agree well with those found in the linear calculations but are larger than those predicted by Nguyen et al. (2012). The disagreement with previous LSA results could be attributed to resolution. It has been recently shown that lens-shaped vortices in this regime can be stabilized by modifying the vortex profile (Sutyryn and Radko 2016), which could explain how small  $\text{Bu}$  Meddies persist for long times.
- (iii) Vortices on the order of the deformation radius ( $\text{Bu} \approx 1$ ) are stable in the linear stability calculations, agreeing with Nguyen et al. (2012) and the nonlinear simulations.

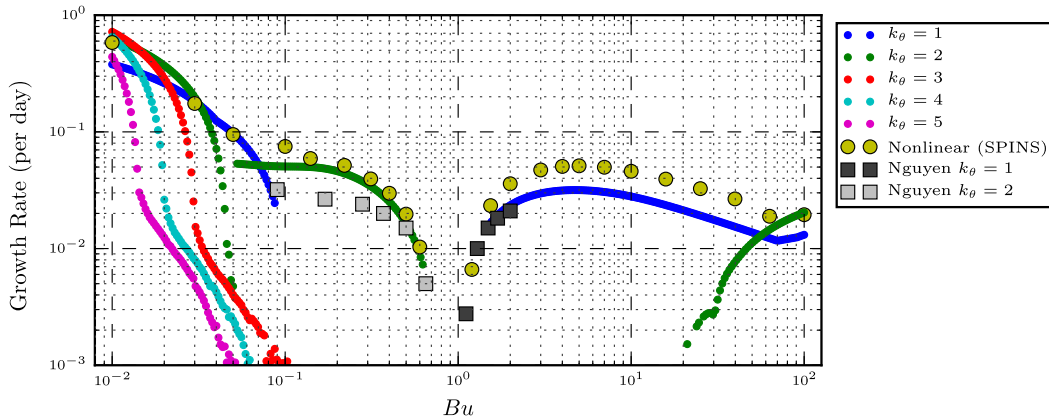


FIG. 1. Linear stability analysis. Results from linear stability analysis (points), nonlinear simulations (yellow circles), and estimates of the [Nguyen et al. \(2012\)](#) result (squares).

(iv) Vortices smaller than the deformation radius ( $1 < \text{Bu} < 10$ ) have an unstable mode with a mode-1 azimuthal structure. In this case the growth rates predicted by the LSA agree with the predictions of [Nguyen et al. \(2012\)](#), but are significantly smaller than those observed in the nonlinear simulations. The nonlinear simulations used a three-dimensional Cartesian coordinate system and only imposed boundary conditions in the far field, in contrast to the cylindrical coordinates used in the linear stability problem. As discussed in [Ash and Khorrami \(1995\)](#), the geometry of the problem means that the  $k_\theta = 1$  mode alone can present nonzero flow at  $r = 0$ , a feature that is present in the nonlinear simulations but not the linear stability calculations. Further, in the nonlinear simulations the perturbation streamfunction grows exponentially along  $r = 0$  at a rate that is roughly comparable to the instability growth rate. A strict  $k_\theta = 1$  mode could not present this, since an odd mode necessarily vanishes at the origin. As will be discussed in [section 5](#), the instability in this regime produces vortex tilting through depth-varying horizontal translations of the vortex. These translations/tilting cause the vortex axis to become distinct from the  $r = 0$  axis, producing nonzero streamfunction perturbations along  $r = 0$ . Since the reference axis has changed, the original projection onto azimuthal modes becomes invalid, suggesting that linear stability analysis using azimuthal decomposition is inherently flawed when considering  $k_\theta = 1$  modes. We have also solved the linearized QG equations in a modified version of QG SPINS in order to capture the true most unstable mode. Unfortunately, our preliminary investigations have only recovered the same mode as is predicted from the LSA, which perhaps suggests that nonlinearity is

important in the dynamics. This is something that we will investigate in future work.

(v) For very thin vortices ( $\text{Bu} > 10$ ) both  $k_\theta = 1, 2$  are unstable. The growth rates from the nonlinear simulations agree with the LSA for the two rightmost points, for which the  $k_\theta = 2$  mode is dominant.

These results agree qualitatively with [Mahdinia et al. \(2016\)](#), who found that for  $|\text{Ro}| \ll 1$  the dominant instability transitions from a symmetric  $k_\theta = 2$  mode when  $\text{Bu} < 1$  to an asymmetric  $k_\theta = 1$  mode when  $\text{Bu} > 1$ . When  $\text{Bu} \ll 1$ , [Mahdinia et al. \(2016\)](#) predict the return of an asymmetric  $k_\theta = 1$  mode. Our linear stability results confirm that an asymmetric mode-1 instability does arise for  $\text{Bu} \ll 1$ . However, taking the Burger number smaller still ( $\text{Bu} \lesssim 0.04$ ), the mode-1 instability is again symmetric and presents an  $(r-z)$  spatial structure similar to the  $k_\theta = 1$  mode of comparable  $\text{Bu}$ . The following section compares the spatial structures with [Yim \(2015\)](#) and [Yim et al. \(2016\)](#) in order to identify the observed instabilities.

#### b. Identification of unstable modes

Barotropic instabilities develop from an unstable horizontal shear and predominantly extract kinetic energy from the background flow. In contrast, baroclinic instabilities occur when perturbations can extract potential energy from a basic state, for which there must be a vertical shear. Rayleigh's theorems give a necessary condition for each type of instability to occur in planar flow ([Pedlosky 1987](#)), and these can be adapted to circular geometries ([Gent and McWilliams 1986](#)). The necessary condition for a vortex in the stratified QG model to be barotropically unstable is that the radial gradient of the background PV, what we call  $\partial_r Q$ , changes sign along the radial direction. In contrast,

the corresponding necessary condition for baroclinic instability in QG is that the radial gradient of the PV changes signs in the vertical direction (Gill 1982, p. 564).

For the particular Gaussian profile under consideration here, both necessary conditions are satisfied for all Bu. However, for large enough Bu, the radius where the sign changes in the vertical is far above the vortex since it is dominated by horizontal shear. Similarly, for small enough Bu the radius at which  $\partial_r Q$  changes sign is far removed from the center because vertical shear is dominant. The change of shear dominance is why, even though the necessary criteria for both barotropic and baroclinic instabilities are satisfied for all Bu, we expect the instabilities for large (small) Bu to be mostly barotropic (baroclinic).

Some care needs to be taken regarding the classification of the unstable modes. This paper follows the nomenclature presented in Yim et al. (2016). A brief description of some of the important unstable modes is provided here. The term Gent–McWilliams mode refers to the barotropic instability that Gent and McWilliams (1986) called an internal mode, or a mode whose maximum growth rate occurs for a nonzero vertical wavenumber. In comparison, baroclinic Gent–McWilliams mode refers to an instability that is characteristically very similar to a traditional Gent–McWilliams mode, but occurs in the regime of baroclinic instabilities ( $Bu < 1$ ), and so is necessarily a baroclinic instability.

The modal structures that are presented here are not new, but are included in order to classify the unstable modes through comparison with Yim et al. (2016). The plots of the unstable modes, Figs. 2 and 3, use color maps provided by Thyng et al. (2016). (These color maps are used later in Figs. 9 and 10). Note that in Figs. 2 and 3 no color bar is shown since the magnitude of the linear modes is not important. However, the color bar is kept consistent across all figures for the purpose of comparison.

- (i) For  $10^{-2} < Bu < 10^{-1}$ , there are two regimes of interest, the transition between which occurs at roughly  $Bu = 0.04$ . Figures 2a,b present the spatial structure of the  $k_\theta = 1$  mode for  $Bu = 0.03$ . Interestingly, the spatial structure of all five computed modes ( $k_\theta \in \{1, 2, 3, 4, 5\}$ ) are qualitatively very similar. Following Yim et al. (2016), this regime corresponds to a baroclinic instability mode. Figures 2c,d show the spatial structure for  $k_\theta = 1$  when  $Bu = 0.05$ . This mode falls within the regime of what Yim et al. (2016) call a baroclinic Gent–McWilliams mode (see their Fig. 39d). In contrast to the baroclinic instability mode, this

mode is vertically asymmetric and has a lower radial mode number.

- (ii) For  $10^{-1} < Bu < 1$ , the only unstable mode corresponds to  $k_\theta = 2$ . Figures 3a,b plot the streamfunction for  $Bu = 0.14$ . This is a baroclinically unstable mode and corresponds to the baroclinic-shear mode, as named by Yim et al. (2016). This is readily verified by comparing these structures with the pressure field in Fig. 5.46 of Yim (2015).
- (iii) For  $1 < Bu < 10$ , consider the unstable mode with  $k_\theta = 1$  and  $Bu = 5$ , the streamfunction of which is presented in Figs. 2e,f. This is the only unstable mode in the range  $1 < Bu < 10$  and is due to the barotropic shear that is dominant in this parameter regime. This mode is asymmetric about the center and is referred to as the Gent–McWilliams mode, as first introduced in Gent and McWilliams (1986) and further studied in Yim et al. (2016). These plots are similar to those of Figs. 2c,d; however, it should be emphasized that the underlying mechanism is a barotropic instability. Correspondingly, this mode is less radially constrained and more vertically constrained than the corresponding Baroclinic Gent–McWilliams mode. Note that the streamfunction agrees qualitatively with the pressure field in Fig. 5.43 of Yim (2015).
- (iv) For  $10 < Bu < 100$ , both  $k_\theta = 1$  and  $k_\theta = 2$  are unstable. Figures 2g,h plot the streamfunction of the most unstable  $k_\theta = 1$  mode for  $Bu = 100$ . It is readily seen that the mode is symmetric about the center, in contrast to  $Bu = 5$ , but more importantly there are much smaller vertical scales that develop near the top and bottom of the vortex, with the mode vanishing near the vortex core. Figures 3c,d present the spatial structure of the  $k_\theta = 2$  instability in this regime. This mode is barotropic in nature, again based on the stability criteria previously mentioned. The real part of this is very similar to the shear mode studied in Yim et al. (2016).

#### 4. Impact of the Burger number on nonlinear evolution

By using sufficiently small perturbations, typically six to eight orders of magnitude smaller than the basic state extrema, the simulated instabilities undergo an exponential growth phase (hereinafter termed the linear regime) in accordance with what is predicted from linear theory, thereby providing a means to confirm predictions of the linear stability analysis. In addition, the three-dimensional simulations provide several other

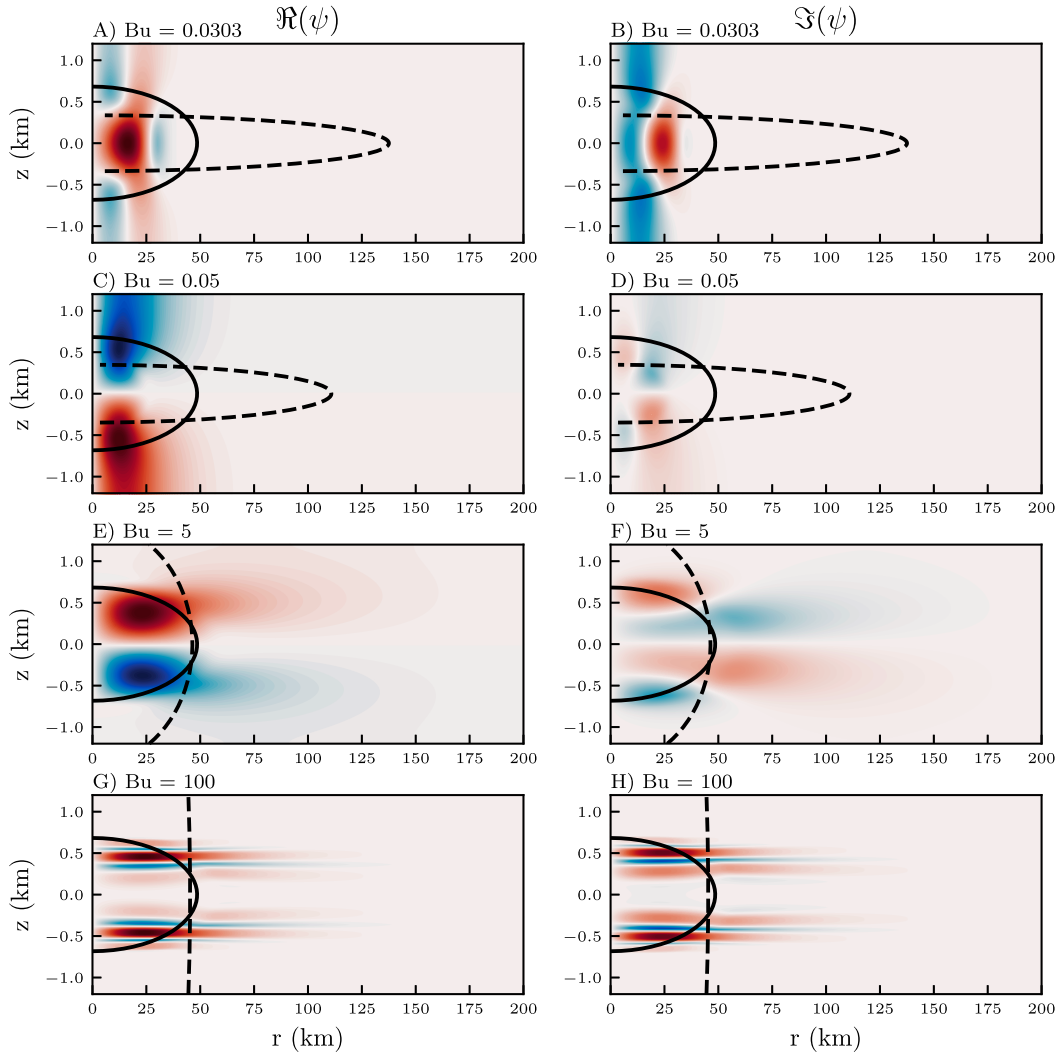


FIG. 2. Contours of the (left) real and (right) imaginary components of the dominant  $k_\theta = 1$  instability for selected Bu values. In each plot the color bar is normalized to  $[-1, 1]$  for comparison. The solid black contour line indicates the 10% streamfunction level. The dashed black contour line indicates when the radial gradient of the background potential vorticity ( $\partial_r Q$ ) changes sign.

diagnostic tools, including three-dimensional renderings of the instability (VisIt; see Childs et al. 2012), measuring the extent and direction of energy transfers, computing wavenumber-dependent rates of change of energy, and quantifying the generation of small-scale energy.

In this section, two nonlinear simulations are presented. The first is a representative for the moderately large Burger regime, with  $Bu = 5$ , corresponding to a 5 km vortex. The second case presented is a representative of the moderately small Burger regime, with  $Bu = 0.14$  and corresponding to a 30-km vortex. While many more nonlinear simulations were performed, these two simulations provide a good representation of

the two primary regions of interest and the corresponding instabilities:  $k_\theta = 1$  for large Bu and  $k_\theta = 2$  for small Bu.

*a. Large Burger number regime*

Figures 4a–d present four three-dimensional renderings of the vortex in various stages of destabilization. Each plot presents volume renderings of potential vorticity  $q$ , where gold denotes anticyclonicity and teal indicates cyclonicity. Note that the displayed aspect ratio differs greatly from the true aspect ratio.

Figure 4a illustrates the initial conditions, in this case with  $Bu = 5$ , hereinafter referred to as the large Burger case. Physically, a large Burger number restricts the

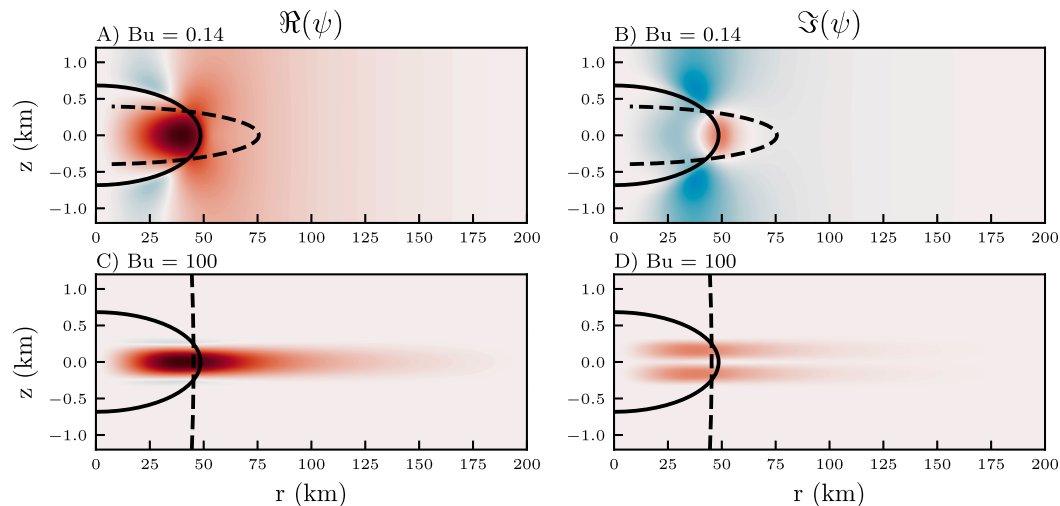


FIG. 3. As in Fig. 2, but for the dominant  $k_\theta = 2$  instability.

amount of vortex tube stretching that can occur. In Eq. (2), this corresponds to decreasing the influence of the vertical derivative of the streamfunction. As a result, the vortex is dominated by horizontal shear, as demonstrated by the initial horizontal shielding of the anticyclonic core by a cyclonic layer.

Figure 4b shows the initial destabilization at the end of the linear regime when the system is transitioning into nonlinear saturation. The anticyclonic core begins to tilt, which results in tail-like features at the vertical periphery as the vortex continues to rotate about the original axis. As the tilted vortex rotates, there is strong tearing, or shedding, of the cyclonic shielding as the strong anticyclonic core interacts with the outer cyclonic layer.

Later, in Fig. 4c, the tails have elongated and have begun to separate from the vortex core, while the shielding deteriorates further. The remnants of the cyclonic shield show interesting spatial patterns at the length scale of the original vortex as well as much smaller-scale filamentary features. Ultimately, Fig. 4d reveals the quasi-steady end state. The tilted anticyclonic core has lost the vertical end tails, which collapsed into small anticyclones. The cyclonic shielding has been greatly reduced, with mostly filamentary structures remaining along the center. The simulation illustrates that for large Burger number, the mode-1 instability results in vortex tilting. Moreover, while the anticyclonic core remains mostly coherent, the cyclonic shielding is mostly removed.

The perturbation potential vorticity, extracted from the linear phase, is presented in Fig. 4e. As anticipated from the linear stability analysis, the mode demonstrates vertical asymmetry and has an azimuthal mode of  $k_\theta = 1$ .

The dominant instability is composed of two twinned cores of opposing polarity in the center, with thinner ribbons wrapping along the vortex periphery. The twinned cores and vertical asymmetry correspond to the vortex tilting, a mechanism that is further discussed in section 5.

Gent and McWilliams (1986) studied the stability of columnar vortices and found that  $k_\theta = 1$  (their  $l = 1$ ) corresponds to an instability with a baroclinic helical vertical structure. The instability presented here is comparable to the Gent–McWilliams  $k_\theta = 1$  instability in that both present baroclinic helical structures, with one difference being the ‘ribbons’ along the vortex periphery in the nonlinear simulation.

#### b. Small Burger number regime

Figures 5a–d present four three-dimensional renderings of the vortex in various stages of destabilization. Since the fields are typically symmetric about the middepth, only the lower half domain is presented in order to provide a more detailed view of the system.

Figure 5a illustrates the initial conditions, a  $Bu = 0.14$  interior vortex. In the small  $Bu$  regime, vortex tube stretching is anticipated to be an important mechanism in contrast to horizontal shear. Indeed, the vortex is dominated by vertical shear, as demonstrated by the trilobe structure in the vertical (recall that only the lower half domain is presented, so the trilobe appears as a 1.5-lobe). That is, for small Burger numbers the cyclonic shielding appears in the vertical, while the shielding is in the horizontal for large Burger numbers.

The initial destabilization of the vortex is shown in Fig. 5b and the formation of arms in both the

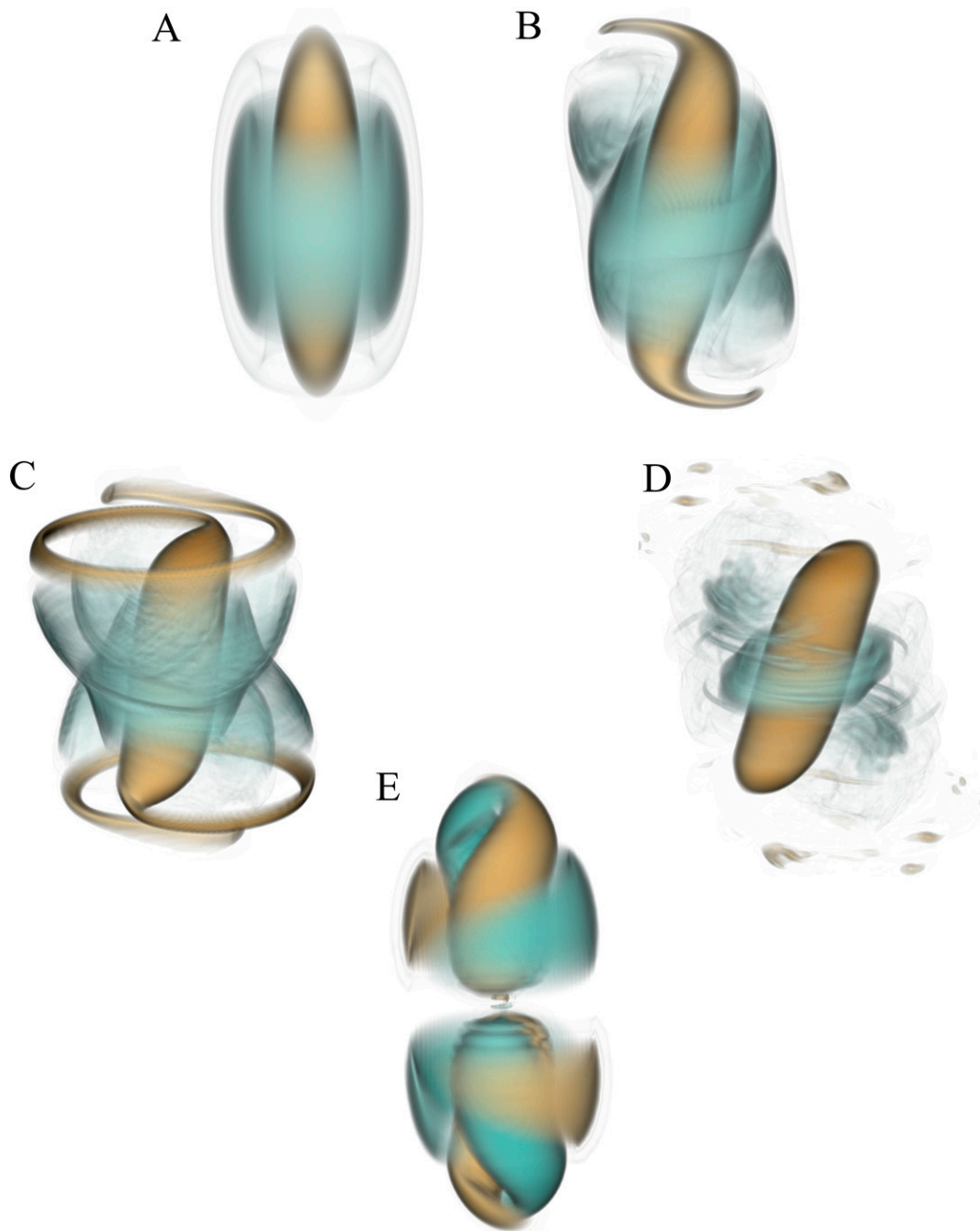


FIG. 4. Three-dimensional plots of a  $Bu = 5$  vortex at select times. Renderings are of the potential vorticity, with gold denoting anticyclonicity and teal denoting cyclonicity. (a) Initial conditions, (b) 570 days, (c) 640 days, (d) 1060 days, and (e) perturbation field at 190 days. Aspect ratio not to scale.

anticyclonic and cyclonic lobes is visible. Ménesguen et al. (2012) present seismic readings that indicate the presence of similar arm features in observed Meddies. Then, Fig. 5c shows that the core vortex has torn into two vortices of roughly equal size, with a trail of small vortices remaining, remnants of the vorticity filament that connected the two new vortices prior to

the tearing event. Ultimately, Fig. 4d reveals the quasi-steady end state in which the initial vortex has been reduced to vortices with greatly reduced horizontal scales. During the linear regime, the dominant unstable mode can be extracted and is presented in Figs. 5e,f. In contrast with Fig. 4e, this mode is primarily restricted to the vortex periphery. Figure 5f,

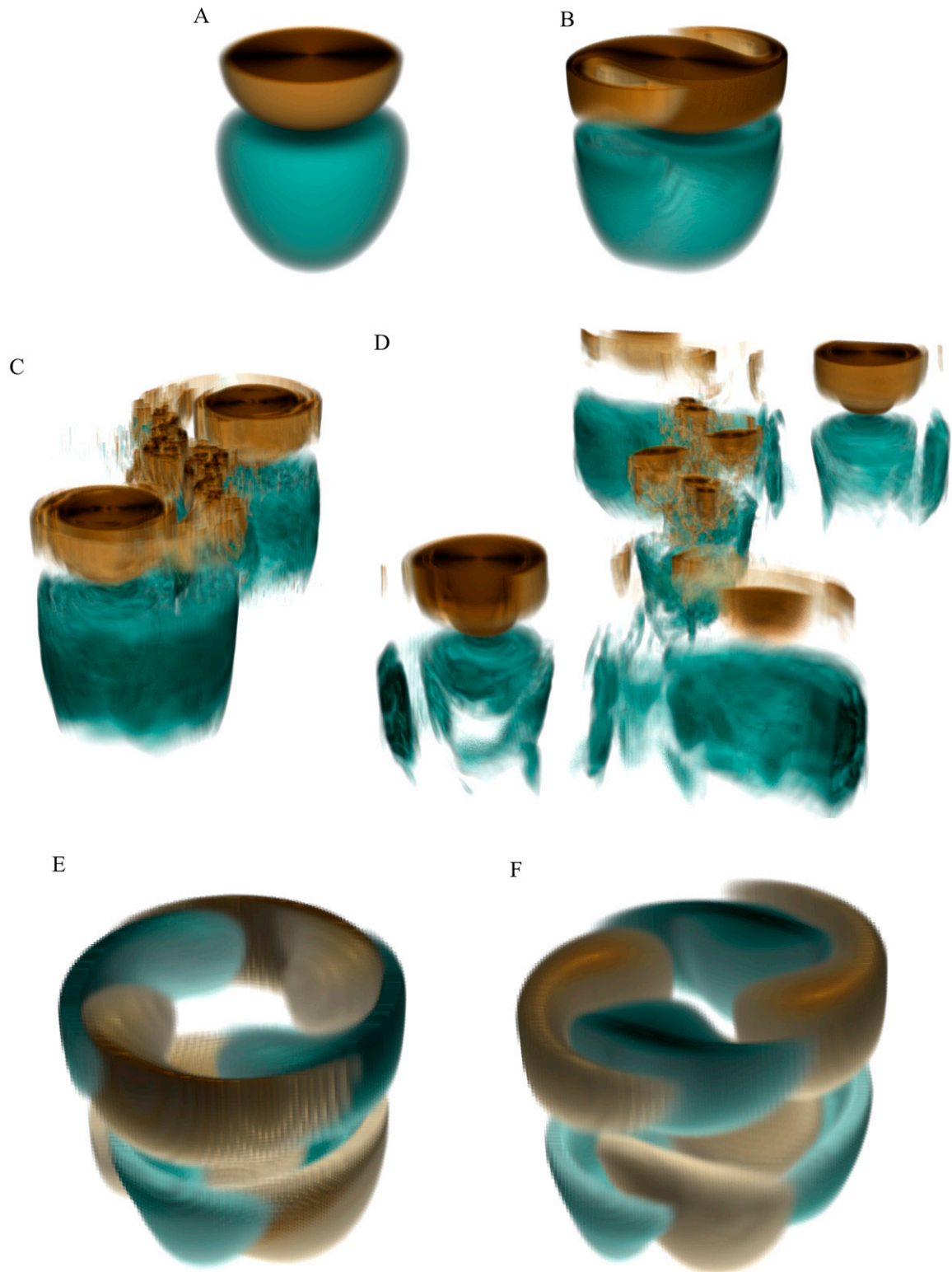


FIG. 5. Three-dimensional plots of the inferior half-domain of a  $Bu = 0.14$  (30 km) vortex at select times. Renderings are of the potential vorticity, with gold denoting anticyclonicity and teal denoting cyclonicity. (a) Initial conditions, (b) 2530 days, (c) 2860 days, (d) 3200 days, (e) perturbations at 1000 days, and (f) perturbations at 2500 days. Aspect ratio not to scale.

which shows the perturbation field at 2500 days, shows how the  $k_\theta = 2$  mode generates the arm structures. This is classified as a baroclinic-shear instability mode (Yim et al. 2016).

*c. Azimuthal decomposition: A comparison with linear theory*

While the growth rates presented in Fig. 1 provide the overall growth rate of the perturbation fields in the nonlinear simulations, it does not distinguish between azimuthal modes. To compute the growth rates of the individual modes, the perturbation field of each three-dimensional simulation is projected onto a cylindrical coordinate basis, where the center of the coordinate system corresponds to the center of the initial vortex. A Fourier transform is applied to the azimuthal dimension to decompose the perturbation into  $k_\theta$  components. The transformed system is then integrated in  $r$  and  $z$  in order to compute the net contribution of each azimuthal mode. That is, for each  $k_\theta$  the contribution  $p(k_\theta)$  of each azimuthal mode is computed as follows:

$$p(k_\theta) = \int_{z=-L_z}^{z=0} \int_{r=0}^{r=L_r} \hat{q}(r, k_\theta, z)^2 dr dz,$$

where  $\hat{q}$  denotes the  $\theta$ -Fourier-transformed potential vorticity perturbation, so that, following Parseval's theorem,  $p(k_\theta)$  measures the  $k_\theta$  component of the perturbation enstrophy  $(q - Q)^2$ . Figure 6 presents a summary of the growth of the first 10 azimuthal modes for a selection of nonlinear simulations. In each plot, the vertical dotted lines indicate the beginning and end of the linear phase, while the vertical dashed line marks an approximation to the nonlinear saturation time. Note that the azimuthal projections may be unreliable after the linear regime, as the vortices may tear or shift, causing the projection to cylindrical coordinates to be inappropriate.

In agreement with the linear stability analysis, the projections show that the large Burger number regime ( $1 < \text{Bu} \leq 10$ ; small vortex widths) is initially dominated by growth of the  $k_\theta = 1$  mode, while small Burger number ( $0.1 \leq \text{Bu} < 1$ ; large vortex widths) is dominated by a  $k_\theta = 2$  mode, and very small Burger number ( $\text{Bu} \leq 0.1$ ; very large vortex widths) demonstrates growth in both  $k_\theta = 1$  and  $k_\theta = 2$  modes. Toward the end of the linear phase, the nondominant modes experience very rapid growth, corresponding to nonlinear interaction.

*d. Main stages of nonlinear QG evolution*

Studying the growth of the total perturbation does not require a projection into cylindrical coordinates, and so in this subsection the full perturbation is considered instead

of individual azimuthal modes. Further, the growth rate of the fastest-growing azimuthal mode in each of the four cases presented in Fig. 6 was compared to those of the full perturbation and the two were found to agree to at least two significant digits. Note that Fig. 6 uses a log scale and that during the linear growth phase the dominant mode is several orders of magnitude stronger than the other modes. The growth-rate diagnostics as well as integrated energy diagnostics are used to describe the different stages of the evolution of the unstable vortices.

Figure 7 presents the evolution of the norms of the full perturbation and associated growth rates (left column) and domain-integrated energetics (right column) for nonlinear simulations with  $\text{Bu} = 5, 0.31, 0.14,$  and  $0.05$ . For the left column, the red curve is associated with the left-hand  $y$  axis and presents the normalized norm of the perturbation:  $(\|q - Q\|_2)/(\|q\|_2 + \|Q\|_2)$ . Correspondingly, the blue curve is associated with the right-hand  $y$  axis and presents the time derivative of the norm of the perturbation scaled by the Rossby number:  $(1/\text{Ro})(d/dt)(\log\|q - Q\|_2)$ . The growth rate is scaled by  $\text{Ro}$  since, following Vallis (2006, p. 207), the dimensionless time  $tf_0$  scales as  $\text{Ro}^{-1}$ . In both metrics,  $q$  refers to the full potential vorticity field, while  $Q$  refers to the initial vortex solution. For the right column, kinetic energy (KE) and potential energy (PE) are computed as follows:

$$\text{KE} = \frac{1}{2}\rho_0 \iiint_V u^2 + v^2 dV = \frac{1}{2}\rho_0 \iiint_V (\partial_x \psi)^2 + (\partial_y \psi)^2 dV,$$

and

$$\text{PE} = \frac{1}{2}\rho_0 \iiint_V \left(\frac{f_0}{N_0} \partial_z \psi\right)^2 dV. \tag{6}$$

In each simulation, the motion is nearly conservative, which is reflected by the fact that the net energy loss is less than 1%.

The vertical dotted lines indicate an estimate for the beginning and end of the linear regime. The vertical dashed line estimates the nonlinear saturation time by finding the time after which the net energetics change by no more than 2.5% in either direction. Meunier et al. (2015) describe three main stages of vortex destabilization: the linear stage, the splitting stage, and the restabilized stage. These stages correspond with what we term the linear stage, the nonlinear transition phase, and the nonlinearly saturated phase.

The first simulation (Fig. 7, top row) corresponds to  $\text{Bu} = 5$ . This system is initially KE dominant and experiences a net transfer to PE. The energy transfer begins after the linear regime ends. As discussed in section 4a, this system is dominated by vortex tilting. As regards the perturbation growth, the system undergoes smooth exponential growth after which the perturbation

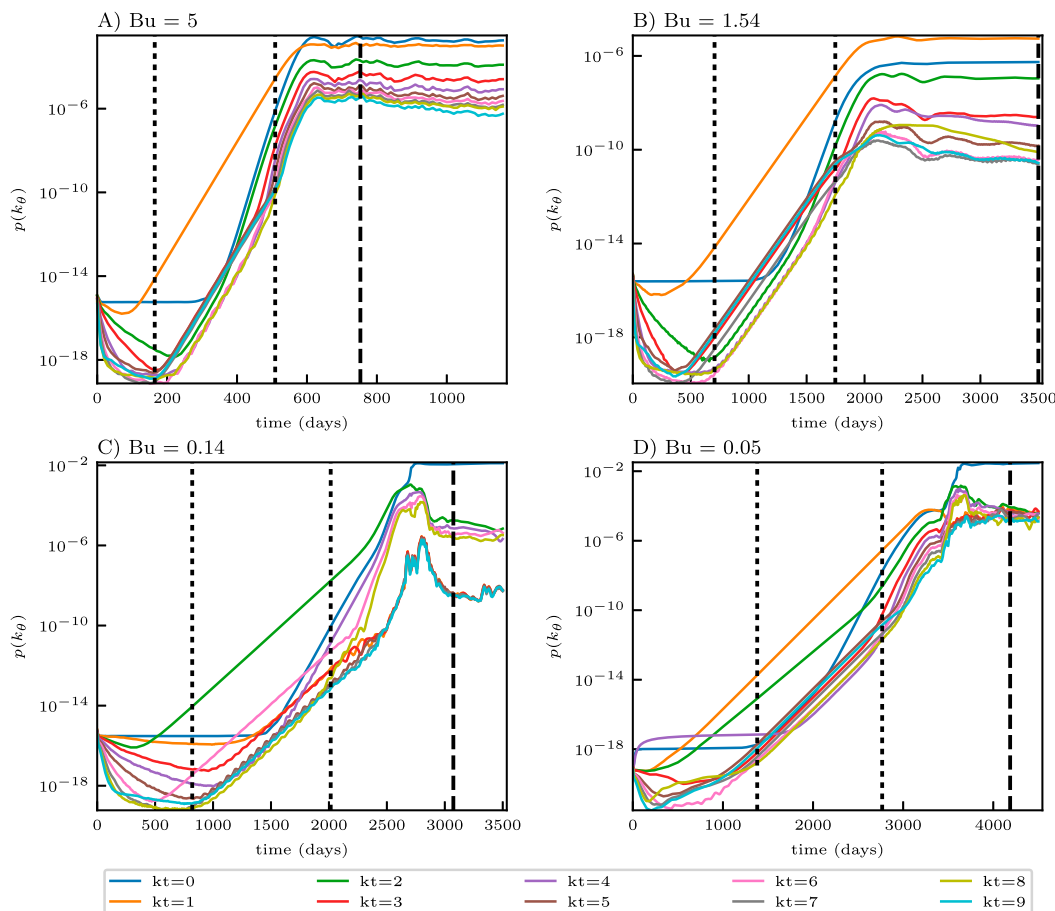


FIG. 6. Azimuthal decompositions for four selected nonlinear simulations, depicting the growth of the separate modes. Burger numbers are given in the figure labels. The vertical dotted lines indicate an estimate for the beginning and end of the linear regime. The vertical dashed line estimates the nonlinear saturation time. The first three subfigures show that the linear theory correctly predicts the most unstable mode that grows initially. The fourth subfigure demonstrates that there are initially two unstable modes.

growth declines and the system enters a quasi-equilibrated regime. The latter three simulations correspond to  $Bu = 0.31, 0.14,$  and  $0.05$ . These cases are initially PE dominant, with the initial disparity increasing as  $Bu$  decreases. In each case, there is a net transfer of PE to KE, corresponding to a baroclinic instability. The last two simulations experience sufficiently strong energy conversions so as to cause a change in the distribution of energy: the quasi-steady regime is KE dominant while the initial state is PE dominant. In these cases, the time of the change in energy dominance corresponds to the vortex tearing event. The  $Bu = 0.31$  simulation, in contrast, remains PE dominant in the quasi-steady regime and does not undergo vortex splitting. In each of these cases, the linear regime terminates in a rapid but brief increase of the perturbation growth rate. The spike in the perturbation growth rate is associated with the formation of the arms as seen in Fig. 5a.

Figure 8a provides measures of how large the instability grows before the system reaches nonlinear saturation. The black curves plot the magnitude of the nonlinearly saturated perturbation norms, while the magenta and cyan curves, respectively, plot the net amount of PE and KE transferred. For  $Bu < 1$ , the system is characterized by a conversion of PE to KE; in contrast, for  $Bu > 1$  the system demonstrates a KE to PE transfer. These are respectively indicative of a baroclinic and barotropic instability.

Interestingly, the barotropic-type instability for  $1 < Bu < 10$  demonstrates much weaker energy conversion than the baroclinic instability for  $10^{-1} < Bu < 1$ , despite the two instabilities having comparable growth rates in the nonlinear simulations. Additionally, the proportion of converted energy for  $Bu > 1$  increases when the  $k_\theta = 2$  instability returns. Combined, these results suggest that it is not simply that baroclinic

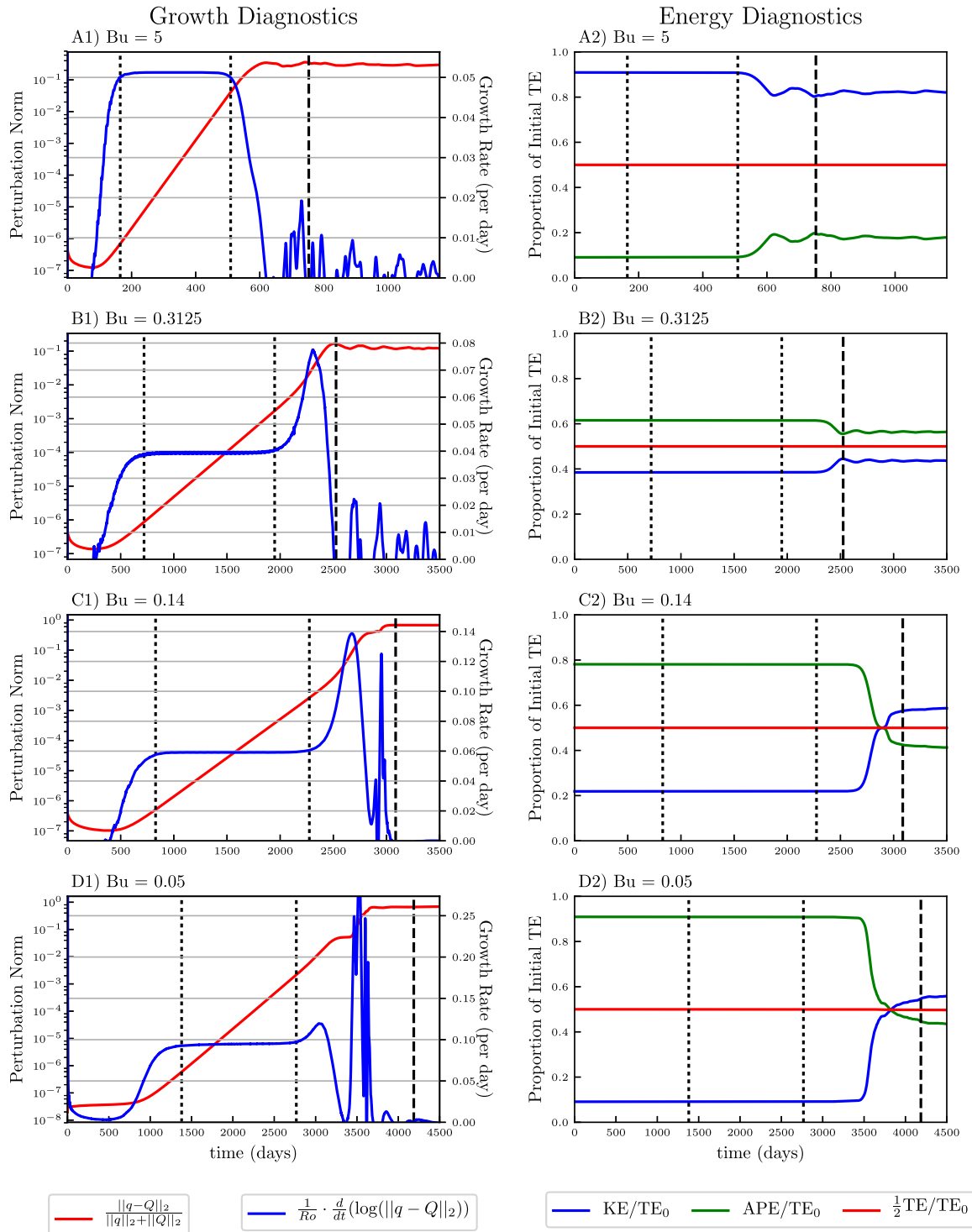


FIG. 7. Growth rates of the (left) full perturbation and (right) nondimensional energies for four nonlinear QG simulations. Burger numbers are given in figure labels. In (left), the red curves indicate the perturbation norms and the blue curves outline the growth rates. These growth rates are included in Fig. 1 as “nonlinear (SPINS)” (i.e., yellow circles). For (right), the blue, green, and red curves denote KE, PE, and half the total energy, respectively, each normalized by the initial total energy. The vertical dotted lines indicate an estimate for the beginning and end of the linear regime. The vertical dashed line estimates the nonlinear saturation time by finding the time after which the net energetics change by no more than 2.5% in either direction.

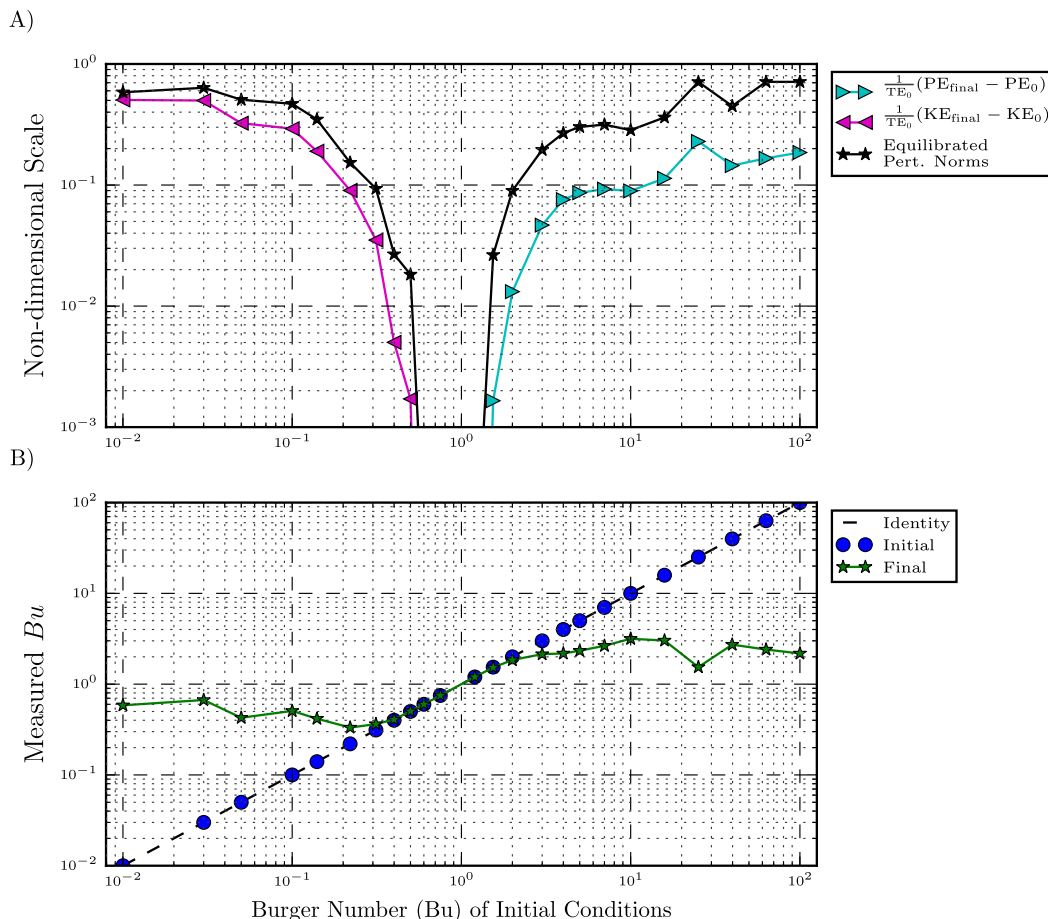


FIG. 8. (a) Net energy conversions (cyan and magenta) and final perturbations norms (black). For the energy transfers, magenta indicates net KE production while cyan indicates net PE production. This reinforces the idea that baroclinic instabilities correspond to  $Bu < 1$  while barotropic instabilities occur for  $Bu > 1$ . (b) The initial and terminal Burger number for each nonlinear simulation.

instabilities are stronger at converting energy than barotropic instabilities, but instead that the  $k_\theta = 2$  mode is able to convert more energy than the  $k_\theta = 1$  mode.

The norms of the nonlinearly saturated perturbation show qualitatively similar behavior to the net energy transfers. However, in the case of vortex splitting, the nonlinearly saturated perturbation may not be meaningful as the system has deviated too strongly from the initial condition.

Figure 8b plots the initial and terminal global Bu for the system. For these purposes,

$$Bu_{\text{measured}} \approx \frac{1}{2} \frac{KE}{APE} = \frac{1}{2} [(\partial_x \psi)^2 + (\partial_y \psi)^2] \left( \frac{f}{N_0} \partial_z \psi \right)^{-2}.$$

That the blue dots, which indicate the initial Burger number under this metric, coincide with the identity function serves to validate the metric. The dynamics

can be divided into three regimes. For  $Bu \approx 1$ , there is no discernible change in Bu, corresponding with the stability of the system. When  $Bu < 1$ , the horizontal vortex scale exceeds the deformation radius, and the baroclinic instability acts to reduce the horizontal scales and a net decrease in Bu (Gent and McWilliams 1986). It is interesting to note that, while the instability always serves to drive the system toward the stable neighborhood of  $Bu = 1$ , stronger instabilities drive the system closer to  $Bu = 1$  than weak instabilities. As mentioned, the vortex tearing events for  $k_\theta = 2$  and  $Bu < 1$  correspond to the energy parity event, when  $KE = APE$ . This suggests that  $Bu_{\text{measured}} = 0.5$  is the Burger number during the vortex tearing event.

There are four major results in this subsection. First, the Gent–McWilliams and shear instabilities for  $Bu > 1$  have a net conversion of KE to PE, while the baroclinic-shear and baroclinic instabilities for  $Bu < 1$  have a conversion of PE to KE. Second, instabilities in the limit of very small  $Bu$  convert a greater proportion of initial total energy than in the limit of very large  $Bu$ . Third, in the simulation of the instability with  $k_\theta = 2$  presented here, the energy parity event corresponds to the tearing event. Finally, sufficiently strong instabilities drive the system toward  $Bu = 1$ , which is stable, and stronger instabilities can drive the system closer to  $Bu = 1$  than weaker instabilities. This implies that the instability events tend to generate structures whose horizontal length scales are commensurate to the Rossby radius of deformation.

#### *e. Spectral distribution of energy and energy transfers*

Figures 9 and 10 present the wavenumber-dependent time rate of change of the potential and kinetic energies for the large and small Burger number vortices corresponding to Figs. 4 and 5. Figure 9 is restricted to only consider the linear regime (the portion between the vertical dotted lines in Fig. 7), while Fig. 10 considers the nonlinear portion of the simulation (everything after the second vertical dotted line in Fig. 7). In each plot, the vertical axis is time and the horizontal axis represents inverse horizontal length scale. To produce the spectra, the full three-dimensional power spectra were azimuthally integrated and depth averaged to produce a mean horizontal power spectrum. The vertical cyan, magenta, and black lines indicate the vortex length  $L_h$ , the deformation radius  $L_D$ , and the filter cutoff, respectively. The horizontal dashed line indicates the estimated nonlinear saturation time, as in Fig. 7.

Note that Figs. 9 and 10 each use two different logarithmic scales, with red (blue) indicating that energy is increasing (decreasing) in time. In each of Figs. 9 and 10, the upper row corresponds to the large Burger case, while the lower row corresponds to the small Burger case.

Recall that the large  $Bu$  case presents a net transfer of KE to PE. Throughout the linear regime (Figs. 9a,b), KE increases at deformation scales and decreases at vortex scales, while PE increases at both deformation and vortex scales. Both KE and PE present positive energy fluxes to smaller scales. The beginning of the nonlinear regime (Figs. 10a,b) is marked with a positive flux toward small scales in both KE and PE, the magnitudes of which well exceed the generation of small scales presented in Figs. 9a,b. At the conclusion of the downscale energy flux, the system enters into a quasi-steady regime, in which PE alternates between

increasing and decreasing at all scales. While KE demonstrates similarly periodic features, the sign of the flux alternates between subvortex scales and superdeformation scales.

The lower rows, Figs. 9c,d and 10c,d, present the spectra for the small Burger case shown in Fig. 5. The fluxes in the linear regime are characterized by a loss of PE and gain of KE at vortex and supervortex scales, as well as a gain of both KE and PE at subvortex scales. In the nonlinear regime, there is a loss of PE and a gain of KE at the vortex scale. Similar to the large  $Bu$  case, the system demonstrates a positive energy flux toward small scales within the nonlinear transition regime, with the small-scale generation reaching smaller scales for kinetic energy than potential energy; the positive flux to small scales can be seen in Fig. 10 in the red regions at scales smaller than the vortex length. Leading up to the production of small scales, the small  $Bu$  system exhibits a loss of PE and gain of KE at supervortex lengths and a gain of both KE and PE at superdeformation and subvortex lengths. These fluxes correspond to the loss of energy at large length scales and the production of energy at small length scales as a result of the vortex splitting event. Again, similar to the large  $Bu$  case, in the quasi-steady regime the small  $Bu$  case exhibits temporally periodic oscillations in flux. However, in the small  $Bu$  case the oscillations change sign more rapidly with both time and wavenumber than in the large  $Bu$  case. The oscillating fluxes below the deformation scale are significantly weaker and oscillate with a higher frequency than the fluxes above the deformation scale. In total, there is a noticeable increase in large-scale KE and loss of PE at large scales over the duration of the simulation.

Figure 11 presents a time mean of the spectral energy fluxes during the linear regime, which corresponds to the times shown in Fig. 9, for a selection of simulations. Note that the horizontal axis is held constant across each plot for the purpose of comparison and that the spectra do not necessarily span the whole domain for each plot. As a result, the vertical magenta lines, which indicate the respective deformation radii, are aligned.

For each simulation, the fluxes during the linear and first portion of the nonlinear phases (the portion before the termination of the positive flux toward small scales) demonstrate qualitatively similar flux patterns (not shown). The main distinction is that, as seen in Figs. 9 and 10, the strength of the fluxes in the nonlinear regime are several orders of magnitude stronger than the fluxes in the linear regime. This suggests that the linear phase simply “initializes” the instability but does not significantly impact the energetics.

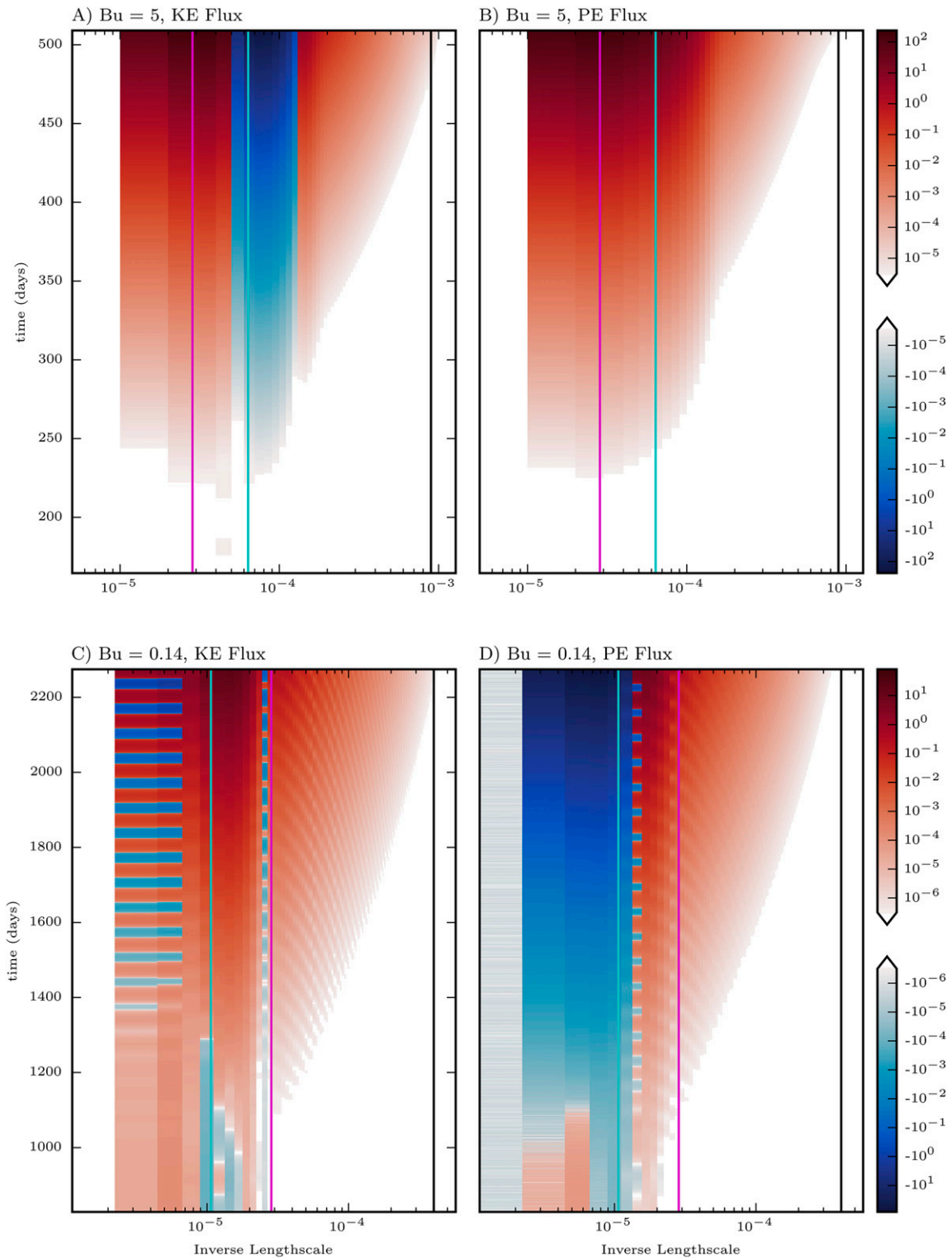


FIG. 9. Wavenumber-dependent time rate of change of (left) kinetic energy and (right) potential energy for (top)  $Bu = 5$  and (bottom)  $Bu = 0.14$  during the linear regime. In each plot, the horizontal axis is inverse length scale ( $m^{-1}$ ) and the vertical axis is time (days). Note that the color bar is divided into a positive (red) and negative (blue) log scale. The vertical cyan, magenta, and black lines indicate the vortex length, the deformation radius, and the filter cutoff, respectively.

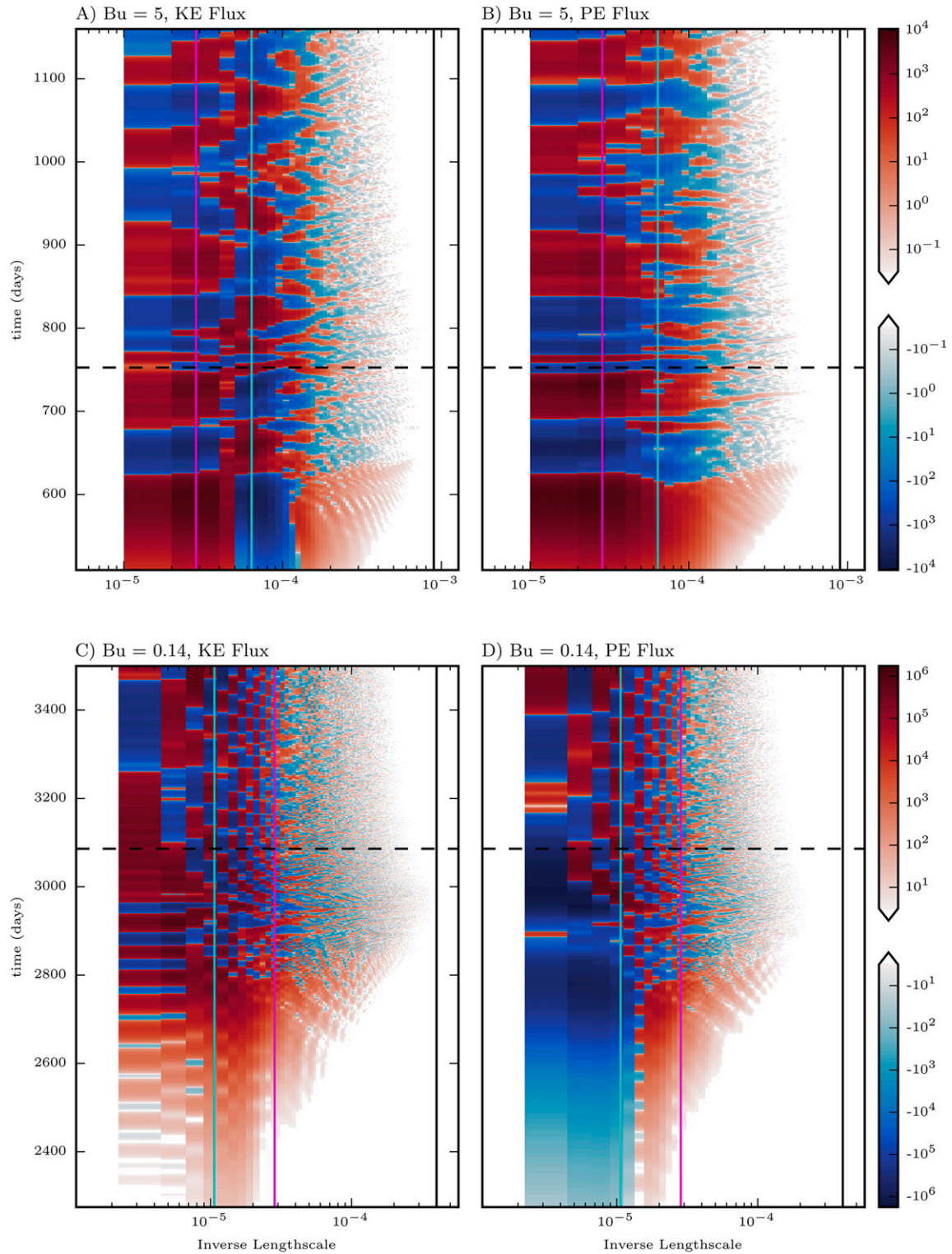


FIG. 10. Wavenumber-dependent time rate of change of (left) kinetic energy and (right) potential energy for (top)  $Bu = 5$  and (bottom)  $Bu = 0.14$  after the linear regime ends. In each plot, the horizontal axis is inverse length scale ( $m^{-1}$ ) and the vertical axis is time (days). Note that the color bar is divided into a positive (red) and negative (blue) log scale. The vertical cyan, magenta, and black lines indicate the vortex length, the deformation radius, and the filter cutoff, respectively. The horizontal dashed line indicates the estimated nonlinear saturation time.

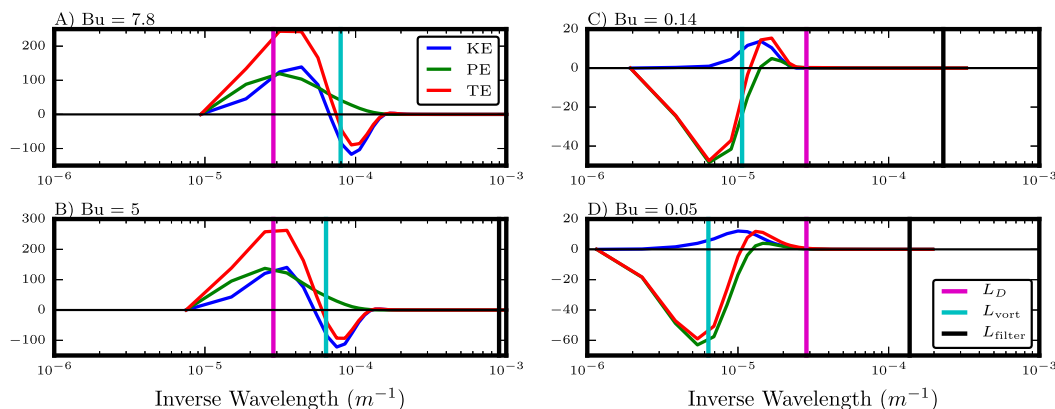


FIG. 11. Time averages of net wavenumber-dependent time rates of change of energy across the full linear phase (as defined in Fig. 7 and illustrated in Fig. 9) for four different Bu values. The solid red, green, and blue curves provide the time-mean flux of total, potential, and kinetic energy, respectively. Vertical cyan lines denote the vortex length, vertical black dotted lines indicate the filter cutoff, and vertical magenta lines identify the vortex length.

For large Bu (Fig. 11, left column) the instability is characterized by a net loss of total energy (TE) and KE at vortex scales, with a corresponding increase of TE, KE, and PE at the deformation scale. The positive flux of energy toward larger scales corresponds to a vortex-tilting mechanism, which increases horizontal length scales. As the vortex scale increases, the wavenumber corresponding to the greatest negative energy flux also increases so that the two remain essentially coincident.

The right column of Fig. 11 corresponds to  $Bu < 1$ . In these cases, there is a loss of TE and PE at scales equal to or greater than the vortex scale, while TE and KE are produced at scales between the vortex length and deformation radius. Some PE is also produced at subvortex scales, but the energy generation is predominantly kinetic. The net energy transfer toward subvortex scales corresponds to a vortex-splitting mechanism, which produces smaller vortices with length scales more comparable to the deformation radius. Further, consider the wavenumber corresponding to the greatest positive energy flux. As the vortex length increases, the wavenumber of greatest positive flux also increases so that it remains roughly halfway (in a logarithmic sense) between the vortex and deformation scales.

In both cases, the nonlinear dynamics create a strong positive energy flux to small scales in both KE and PE. Figure 12 presents three quantifications of the production of small scales: the proportion of energy in length scales smaller than one-third of the vortex scale (blue squares), smaller than one-fifth of the vortex scale (orange asterisks), and smaller than the deformation radius (magenta triangles). When  $Bu > 1$ , the vortex itself is smaller than the deformation radius, and so the third metric is not meaningful. Note that the figure uses a log scale. The two

vortex-based metrics show two main trends. The  $Bu < 1$  instabilities tend to be able to produce significantly more subvortex-scale energy than when  $Bu > 1$ , corresponding to a bias toward generating deformation-scale energy. Further, subvortex-scale production increases as Bu deviates from 1, suggesting that larger vortices, which correspond to higher growth rates, also demonstrate a downscale energy flux that reaches a wider range of wavenumbers. In contrast, the deformation-scale metric is maximized on  $10^{-1} \lesssim Bu \lesssim 3 \times 10^{-1}$ . Above that, the amount of produced small scales decreases rapidly with increasing Bu, corresponding to the stabilization of the system. Below  $Bu = 0.1$ , the amount of produced small-scale energy increases weakly with Bu.

We are not able to provide a definitive explanation as to why  $Bu \in [0.1, 0.4]$  maximizes the generation of subdeformation radius energy. The spatial structure of the unstable modes do not present significant changes in small-scale features, which is why the subdeformation scale energy that is created must arise because of the nonlinearity of the system. This is not something that can be described in the context of linear theory and is beyond the scope of our manuscript to explain this observation. A scale argument may help to explain why there is a region with maximized subdeformation-scale generation: as Bu decreases, the separation between the vortex scale and the deformation scale increases, and so a stronger energy transfer is required to produce subdeformation energy for smaller Bu.

## 5. Conclusions and discussion

LSA is conducted using both high spatial and parametric resolution and is compared to both Nguyen et al. (2012) and nonlinear simulations. It is determined that

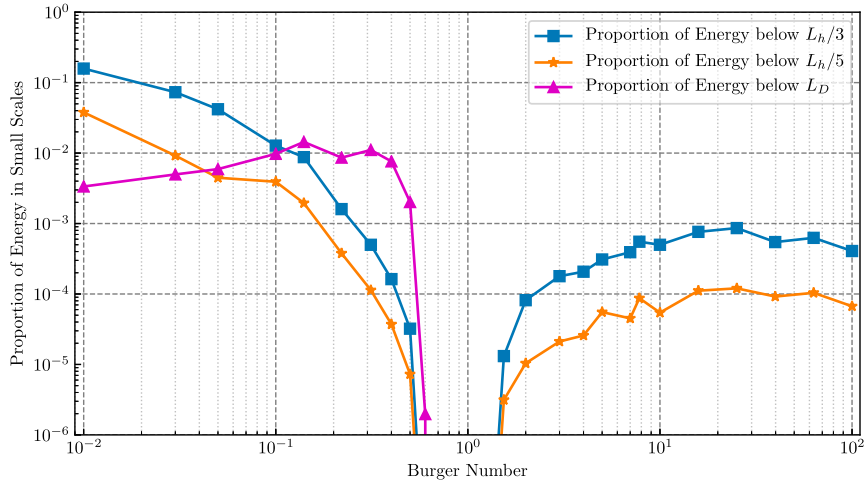


FIG. 12. Three metrics for the production of small-scale energy. Points indicate the proportion of initial total energy that is at scales equal to or less than one-third of the vortex scale (blue squares), one-fifth of the vortex scale (orange asterisks), or the deformation radius (magenta triangles), at the end of the simulation.

there are four different instability regimes. For moderately small  $Bu$  ( $10^{-1} < Bu < 1$ ), the linear and nonlinear results are in good agreement, but differ from the growth rates predicted by [Nguyen et al. \(2012\)](#) for decreasing  $Bu$ , a discrepancy that is explained by the requirement for high resolution to accurately resolve the finescale features. For moderately large  $Bu$  ( $1 < Bu < 10$ ), the presented LSA agrees well with [Nguyen et al. \(2012\)](#), but both LSA calculations disagree with the nonlinear simulations. As discussed in section 3a(iv), this is in part caused by the additional condition that is imposed on the perturbation at the center of the vortex. Comparison with the linear modes presented by [Yim et al. \(2016\)](#) revealed that the instabilities in those regimes are the baroclinic shear instability and Gent–McWilliams instability, respectively. Further, the presented LSA considered an expanded range of  $Bu$ :  $10^{-2} < Bu < 10^2$ . For very large  $Bu$  ( $Bu > 10$ ), the  $k_\theta = 2$  mode is again unstable, for which the LSA agrees with the nonlinear calculations, reinforcing that the discrepancy is inherent to the  $k_\theta = 1$  mode. For very small  $Bu$  ( $Bu < 0.1$ ), all of the computed azimuthal modes are unstable, and it is anticipated that higher azimuthal modes are also unstable.

For moderately small Burger numbers ( $0.1 < Bu < 1$ ), or moderately large vortex scales, the dominant instability is vertically symmetric about the vortex center, has azimuthal mode 2, and, following the nomenclature of [Yim et al. \(2016\)](#), is a baroclinic shear instability. When the instability is sufficiently strong, as illustrated in [Figs. 5e,f](#), the  $k_\theta = 2$  mode causes the formation of arms and a pinching of the vortex core, which can lead to vortex splitting. When a splitting does occur, it corresponds to

parity between kinetic and potential energy. Vortices in this regime have horizontal scales that exceed the deformation radius; as a result, vortex tearing produces vortices on scales that are more commensurate with the first deformation radius. The small  $Bu$  instability is characterized by a net transfer of potential energy into kinetic energy, which is consistent with a baroclinic instability. Corresponding to the decrease in horizontal scales, there is an overall transfer of energy from vortex scales and larger toward subvortex and superdeformation scales ([Fig. 11](#)).

Moderately large Burger numbers ( $1 < Bu < 10$ ), or moderately small vortex scales, contrastingly present a dominant instability that is vertically asymmetric about the vortex center, has azimuthal mode 1, and is a Gent–McWilliams instability (following [Yim et al. 2016](#)). The  $k_\theta = 1$  mode strengthens one side of the vortex while weakening the other, which yields an effect similar to horizontal translation. As a result of the vertical asymmetry, the upper portion of the vortex is translated in the opposite direction of the lower portion, resulting in vortex tilting. Since vortices in this regime have subdeformation horizontal scales and vortex tilting increases horizontal scales, the tilting mechanism produces vortices on scales closer to the deformation radius. Corresponding to the increase in horizontal scales, kinetic and total energy transition from vortex lengths toward deformation lengths, while potential energy is generated at all scales with an emphasis on the deformation radius. Overall, there is a net transfer of kinetic energy into potential energy.

In the small  $Bu$  regime ( $0.1 < Bu < 1$ ) the cyclonic and anticyclonic portions of the vortex undergo similar

evolution. In contrast, the large Bu regime ( $1 < \text{Bu} < 10$ ) has markedly different evolutions for the two portions: the anticyclonic core undergoes vortex tilting, while the cyclonic shielding is heavily dispersed.

As Bu decreases, a greater proportion of the initial energy is transferred to subvortex scales, corresponding to the increased strength of the instability. However,  $10^{-1} \lesssim \text{Bu} \lesssim 3 \times 10^{-1}$  maximizes the amount of subdeformation radius energy that is produced. Here,  $\text{Bu} > 1$  produces significantly less subvortex energy than  $\text{Bu} < 1$ , corresponding to the net upscale energy transfer. We do not have a physical explanation for why  $10^{-1} \lesssim \text{Bu} \lesssim 3 \times 10^{-1}$  maximizes the production of small scales, although it is interesting to note that this regime corresponds with the range for observed Meddies.

Many studies considered Meddies in the context of a Gaussian vortex, and we begin with the same basis, but find that the model is problematic. The observed long-lasting Meddies have Bu considerably less than one, while a Gaussian vortex would be unstable in that regime. Meddies that do not encounter sea mounts can live up to four years (Richardson et al. 2000). In the region  $0.1 < \text{Bu} < 0.3$ , the growth rate estimated by both the presented LSA and nonlinear simulations is approximately  $0.05\text{Ro day}^{-1}$  so the time scale for the instability is 200 days if  $\text{Ro} = 0.1$ . As a result, small (1%) perturbations may yield a lens vortex lifetime of 1000 days, while larger (10%) perturbations may shorten the lifetime to 200–400 days.

Other assumptions made throughout this investigation were the following: the ambient rotation ( $f_0$ ) is very strong compared to that of the vortex, the stratification is strong, and it is only the density that is important, not the temperature–salinity distribution. In future work we will study lens vortices in a primitive equation model, which will allow us to determine the merit in making some of these assumptions. This will allow for a more accurate description of the unstable modes in the very small Burger number regime.

In this manuscript we sought to understand how lens vortices, idealized with a Gaussian streamfunction, destabilize over a wide range of Burger numbers. We began by presenting a more precise view of the linear theory and what growth rates and spatial structures are expected as a function of Burger number. Then, by looking at the nonlinear evolution, we quantify the transfer of energy across the different length scales to better understand how submesoscale features are generated as a function of Burger number. We hope that the combination of these two studies will lead to better parameterizations of unstable lens-shaped vortices that arise in the World Ocean.

*Acknowledgments.* FJP would like to thank NSERC for financial support during the time of this research. BAS would like to thank OGS for financial support during the time of this research. FJP and BAS would both like to thank IFREMER for a kind invitation to visit. We thank Xavier Carton for stimulating conversations about this research. The numerical simulations presented in this paper were performed using the Orca computing clusters provided by SHARCNET and ComputeCanada.

## APPENDIX

### Derivation of Linear Stability Problem

This derivation of the linear stability problem follows Nguyen et al. (2012). The quasigeostrophic potential vorticity equation can be written in terms of the Jacobian  $J$  as follows:

$$\partial_t q + J(\psi, q) = 0.$$

If we assume that the basic state is periodic in the  $\theta$  coordinate, then the basic-state fields can be expressed as follows:

$$\begin{aligned} \psi &= \Psi(r, z), \quad u_r = 0, \quad u_\theta = \partial_r \Psi, \\ q &= Q(r, z) = \frac{1}{r} \partial_r (r \partial_r \Psi) + \frac{f_0^2}{N^2} \partial_{zz} \Psi, \end{aligned}$$

We consider perturbations around this background state in the form:

$$\begin{aligned} \psi &= \Psi(r, z) + \psi'(r, \theta, z, t), \quad \text{and} \\ q &= Q(r, z) + q'(r, \theta, z, t), \end{aligned}$$

as well as assume a normal mode solution, given by

$$[q', \psi'] = \Re\{[\hat{q}, \hat{\psi}](r, z) e^{i(k\theta - \omega t)}\}.$$

Upon substitution into the quasigeostrophic evolution equation and linearizing, we get the normal mode equation in terms of  $\hat{\psi}$  as follows:

$$\begin{aligned} \frac{\omega}{k} \left( \frac{1}{r} \partial_r + \partial_{rr} - \frac{k^2}{r^2} + \frac{f_0^2}{N^2} \partial_{zz} \right) \\ \hat{\psi} = \left[ \frac{1}{r} \partial_r \Psi \left( \frac{1}{r} \partial_r + \partial_{rr} - \frac{k^2}{r^2} + \frac{f_0^2}{N^2} \partial_{zz} \right) - \frac{1}{r} \partial_r Q \right] \hat{\psi}. \end{aligned} \quad (\text{A1})$$

In matrix form, this can be written as the generalized eigenvalue problem:

$$A\hat{\psi} = cB\hat{\psi}, \quad (\text{A2})$$

where  $c = \omega/k$  and

$$A = \left[ \frac{1}{r} \partial_r \Psi \left( \frac{1}{r} \partial_r + \partial_{rr} - \frac{k^2}{r^2} + \frac{f_0^2}{N^2} \partial_{zz} \right) - \frac{1}{r} \partial_r Q \right], \quad (\text{A3})$$

$$= \left( \frac{1}{r} \partial_r \Psi B - \frac{1}{r} \partial_r Q \right), \quad \text{and} \quad (\text{A4})$$

$$B = \left( \frac{1}{r} \partial_r + \partial_{rr} - \frac{k^2}{r^2} + \frac{f_0^2}{N^2} \partial_{zz} \right). \quad (\text{A5})$$

#### REFERENCES

- Aiki, H., and T. Yamagata, 2004: A numerical study on the successive formation of Meddy-like lenses. *J. Geophys. Res.*, **109**, C06020, <https://doi.org/10.1029/2003JC001952>.
- Ash, R. L., and M. R. Khorrami, 1995: Vortex stability. *Fluid Vortices*, S. I. Green, Ed., Kluwer Academic Publishers, 317–372.
- Baey, J.-M., and X. Carton, 2002: Vortex multipoles in two-layer rotating shallow-water flows. *J. Fluid Mech.*, **460**, 151–175, <https://doi.org/10.1017/S0022112002008170>.
- Carton, X., 2001: Modeling of oceanic vortices. *Surv. Geophys.*, **22**, 179–264, <https://doi.org/10.1023/A:1013779219578>.
- Childs, H., and Coauthors, 2012: VisIt: An end-user tool for visualizing and analyzing very large data. *High Performance Visualization: Enabling Extreme-Scale Scientific Insight*, E. Bethel, H. Childs, and C. Hansen, Eds., CRC Press, 357–372.
- Ciani, D., 2016: Tourbillons océaniques intensifiés en subsurface: Signature en surface et interactions mutuelles. Ph.D. dissertation, Université de Bretagne Occidentale, 213 pp.
- , X. Carton, I. Bashmachnikov, B. Chapron, and X. Perrot, 2015: Influence of deep vortices on the ocean surface. *Discontinuity Nonlinearity Complexity*, **4**, 281–311, <https://doi.org/10.5890/DNC.2015.09.006>.
- Gent, P. R., and J. C. McWilliams, 1986: The instability of barotropic circular vortices. *Geophys. Astrophys. Fluid Dyn.*, **35**, 209–233, <https://doi.org/10.1080/03091928608245893>.
- Gill, A. E., 1982: *Atmosphere-Ocean Dynamics*. Academic Press, 662 pp.
- Hua, B. L., C. Ménesguen, S. Le Gentil, R. Schopp, B. Marsset, and H. Aiki, 2013: Layering and turbulence surrounding an anticyclonic oceanic vortex: In situ observations and quasi-geostrophic numerical simulations. *J. Fluid Mech.*, **731**, 418–442, <https://doi.org/10.1017/jfm.2013.369>.
- Mahdinia, M., P. Hassanzadeh, P. S. Marcus, and C.-H. Jiang, 2016: Stability of three-dimensional Gaussian vortices in an unbounded, rotating, vertically stratified, Boussinesq flow: Linear analysis. *J. Fluid Mech.*, **824**, 97–134, <https://doi.org/10.1017/jfm.2017.303>.
- McWilliams, J. C., 1985: Submesoscale, coherent vortices in the ocean. *Rev. Geophys.*, **23**, 165–182, <https://doi.org/10.1029/RG023i002p00165>.
- Ménesguen, C., B. L. Hua, X. Carton, F. Klingelhoefer, P. Schnürle, and C. Reichert, 2012: Arms winding around a Meddy seen in seismic reflection data close to the Morocco coastline. *Geophys. Res. Lett.*, **39**, L05604, <https://doi.org/10.1029/2011GL050798>.
- Meunier, T., C. Ménesguen, R. Schopp, and S. Le Gentil, 2015: Tracer stirring around a Meddy: The formation of layering. *J. Phys. Oceanogr.*, **45**, 407–423, <https://doi.org/10.1175/JPO-D-14-0061.1>.
- Nguyen, H. Y., B. L. Hua, R. Schopp, and X. Carton, 2012: Slow quasigeostrophic unstable modes of a lens vortex in a continuously stratified flow. *Geophys. Astrophys. Fluid Dyn.*, **106**, 305–319, <https://doi.org/10.1080/03091929.2011.620568>.
- Pedlosky, J., 1987: *Geophysical Fluid Dynamics*. Springer, 710 pp., <https://doi.org/10.1007/978-1-4612-4650-3>.
- Prater, M. D., and T. B. Sanford, 1994: A Meddy off Cape St. Vincent. Part I: Description. *J. Phys. Oceanogr.*, **24**, 1572–1586, [https://doi.org/10.1175/1520-0485\(1994\)024<1572:AMOCSV>2.0.CO;2](https://doi.org/10.1175/1520-0485(1994)024<1572:AMOCSV>2.0.CO;2).
- Richardson, P. L., A. S. Bower, and W. Zenk, 2000: A census of Meddies tracked by floats. *Prog. Oceanogr.*, **45**, 209–250, [https://doi.org/10.1016/S0079-6611\(99\)00053-1](https://doi.org/10.1016/S0079-6611(99)00053-1).
- Serra, N., and I. Ambar, 2002: Eddy generation in the Mediterranean undercurrent. *Deep-Sea Res. II*, **49**, 4225–4243, [https://doi.org/10.1016/S0967-0645\(02\)00152-2](https://doi.org/10.1016/S0967-0645(02)00152-2).
- , S. Sadoux, I. Ambar, and D. Renouard, 2002: Observations and laboratory modeling of Meddy generation at Cape St. Vincent. *J. Phys. Oceanogr.*, **32**, 3–25, [https://doi.org/10.1175/1520-0485\(2002\)032<0003:OALMOM>2.0.CO;2](https://doi.org/10.1175/1520-0485(2002)032<0003:OALMOM>2.0.CO;2).
- , I. Ambar, and R. H. Käse, 2005: Observations and numerical modelling of the Mediterranean outflow splitting and eddy generation. *Deep-Sea Res. II*, **52**, 383–408, <https://doi.org/10.1016/j.dsr2.2004.05.025>.
- Subich, C. J., K. G. Lamb, and M. Stastna, 2013: Simulation of the Navier–Stokes equations in three dimensions with a spectral collocation method. *Int. J. Numer. Methods Fluids*, **73**, 103–129, <https://doi.org/10.1002/fld.3788>.
- Sutyryn, G. G., and T. Radko, 2016: Stabilization of isolated vortices in a rotating stratified fluid. *Fluids*, **1**, 26, <https://doi.org/10.3390/fluids1030026>.
- Thyng, K., C. Greene, R. Hetland, H. Zimmerle, and S. DiMarco, 2016: True colors of oceanography: Guidelines for effective and accurate colormap selection. *Oceanography*, **29**, 9–13, <https://doi.org/10.5670/oceanog.2016.66>.
- Vallis, G. K., 2006: *Atmospheric and Oceanic Fluid Dynamics*. Cambridge University Press, 745 pp.
- Yim, E., 2015: Stability of columnar and pancake vortices in stratified-rotating fluids. Ph.D. thesis, École polytechnique Laboratoire d'Hydrodynamique, 176 pp.
- , P. Billant, and C. Ménesguen, 2016: Stability of an isolated pancake vortex in continuously stratified-rotating fluids. *J. Fluid Mech.*, **801**, 508–553, <https://doi.org/10.1017/jfm.2016.402>.
- Zhao, M., and M.-L. Timmermans, 2015: Vertical scales and dynamics of eddies in the Arctic Ocean's Canada Basin. *J. Geophys. Res. Oceans*, **120**, 8195–8209, <https://doi.org/10.1002/2015JC011251>.